

Research Paper

Cite this article: Tsuji E, Aonuma S, Tanaka S (2025) Compact continuous class-F/class-F⁻¹ power amplifiers utilizing one-port CRLH transmission lines for broadband harmonic matching. *International Journal of Microwave and Wireless Technologies*, 1–14. <https://doi.org/10.1017/S1759078725000194>

Received: 2 June 2024

Revised: 24 January 2025


Accepted: 29 January 2025

Keywords:

class-F; CRLH transmission lines; power amplifier; power efficiency

Corresponding author: Shinichi Tanaka;
Email: s-tanaka@shibaura-it.ac.jp

Compact continuous class-F/class-F⁻¹ power amplifiers utilizing one-port CRLH transmission lines for broadband harmonic matching

Eri Tsuji, Soshi Aonuma and Shinichi Tanaka 

Shibaura Institute of Technology, Tokyo, Japan

Abstract

We present continuous Class-F (CCF) and continuous Class-F⁻¹ (CCF⁻¹) power amplifiers (PAs) with compact circuit sizes. The output matching network (OMN) of a continuously harmonic-tuned PA must accommodate varying load impedance conditions across a wide frequency range, spanning from the fundamental frequency up to the 2nd and 3rd harmonic frequencies. This requirement typically leads to LPF-type OMNs with a significant circuit area overhead, thereby limiting the applicability of the broadband PAs. In this paper, we propose utilizing a one-port composite right-/left-handed transmission line to control the harmonic loads, while the fundamental loads are managed by a moderately sized LPF. This resulted in a notable reduction in PA size by nearly an order of magnitude. We demonstrate the effectiveness of this design approach through the fabrication of 2-GHz-band GaN HEMT PAs operating in CCF and CCF⁻¹ modes. While both PAs exhibited high-efficiency (>70%) operational bandwidths at a state-of-the-art level, we also elucidate key design considerations specific to each PA operation mode.

Introduction

With the advancement of mobile communication technologies, the demand for higher efficiency and wider bandwidth in RF transmitters necessitates advancements in power amplifiers (PAs). Over the past decade, the continuous harmonic tuning technique for broadband high-efficiency PAs [1] has received significant attention. Various types of PAs, such as those operating in continuous Class-F (CCF) [2–5] and continuous inverse Class-F (CCF⁻¹) [5–8], have been demonstrated. To accommodate even wider frequency bands, techniques like Class-F⁻¹/Class-F mode transferring have also been explored [9, 10].

Figure 1 depicts the schematic illustrations for continuous harmonic-tuned PAs. The output matching network (OMN) of the continuous mode PA is required to adapt to continuously varying load impedance conditions over a wide frequency range. Specifically, the OMN is required to match the impedance of the fundamental frequency (f_0) inside the Smith Chart, while at the same time providing optimum harmonic loads on the edge of the Smith Chart. Consequently, a multistage stepped-impedance LPF topology is typically utilized for the OMN. Furthermore, to facilitate rapid transition from the impedances for the f_0 -band to those for the $2f_0$ -band, a stepped impedance LPF structure using very low impedance sections become frequently necessary, resulting in a significant footprint for the circuit. Figure 2 shows the correlation between the bandwidth for high-efficiency operation (>70%) and the effective circuit area for state-of-the-art PAs operating in CCF [2, 4], CCF⁻¹ [5, 8], continuous CCF/CCF⁻¹ [9, 10], and conventional Class-F modes [11, 12]. While the CCF and CCF⁻¹ PAs from previous works showcased significant enhancement of the bandwidth compared to conventional Class-F PAs, the circuit area increased by three to five times due to the matching network with LPF topology. Apart from the issue of circuit size, another concern regarding continuously harmonic-tuned PA is the uncertainty surrounding which operation mode, CCF or CCF⁻¹, provides greater advantages. This concern arises because, as [13] highlighted, unlike Class-F⁻¹ PA, Class-F PA experiences a reduction in the high-efficiency operational bandwidth unless the second harmonic source impedance is meticulously managed. On the other hand, under the condition that the harmonics are tuned only up to the 3rd order, the theoretically achievable peak efficiency is higher for Class-F PA (90.7%) [2] compared to Class-F⁻¹ PA (81.9%) [5]. While a comparative evaluation between the two PA modes is not straightforward, there have been few reports that have conducted direct comparisons of CCF and CCF⁻¹ PAs, designed and fabricated under similar conditions.

© The Author(s), 2025. Published by Cambridge University Press in association with The European Microwave Association. This is an Open Access article, distributed under the terms of the Creative Commons Attribution licence (<http://creativecommons.org/licenses/by/4.0>), which permits unrestricted re-use, distribution and reproduction, provided the original article is properly cited.

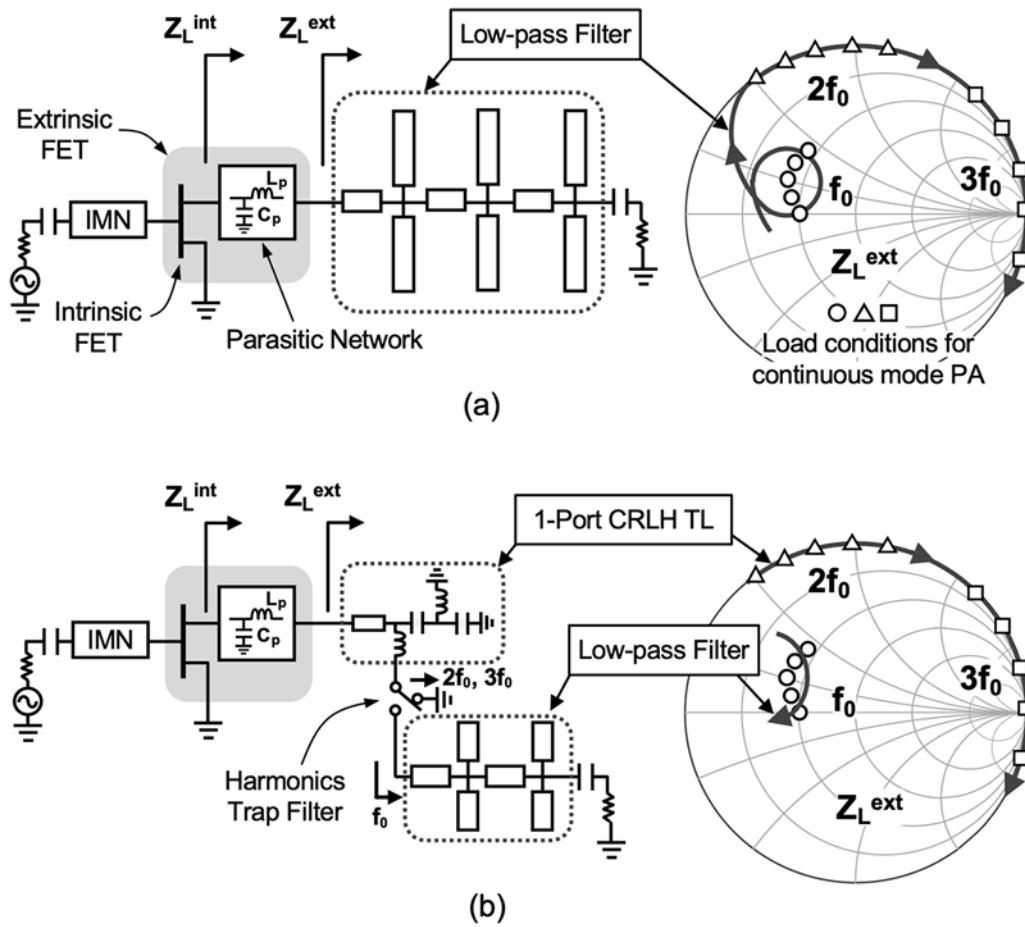


Figure 1. Comparison of continuous mode PAs with (a) conventional and (b) proposed circuit configurations.

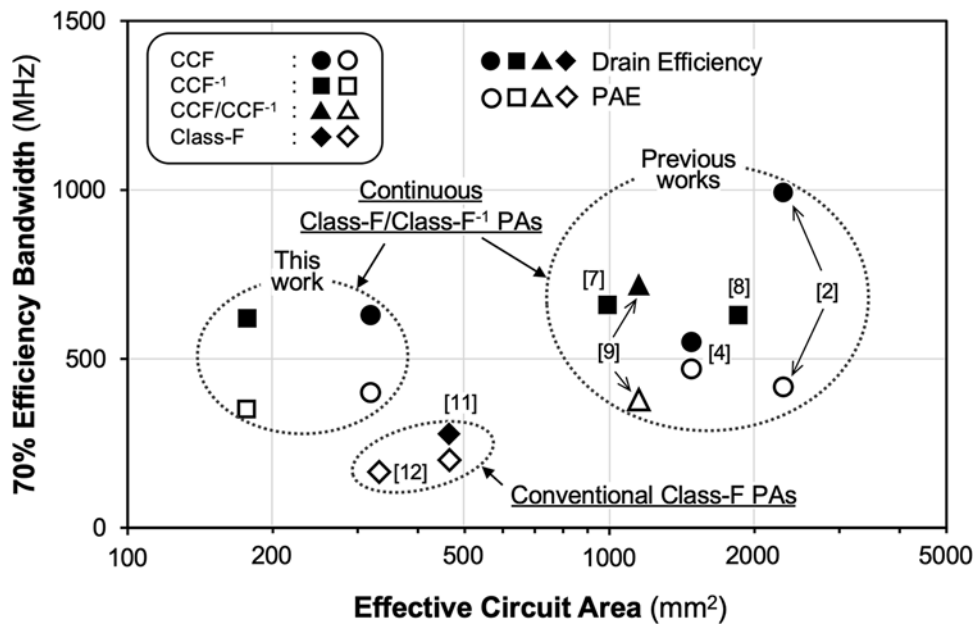


Figure 2. Correlation between bandwidth and effective circuit area for state-of-the-art high-efficiency PAs.

In this paper, we present a novel design approach for continuous mode PAs aimed at significant reduction in their circuit size, thereby expanding their applicability. The proposed PA leverages the extremely compact size and the flexible harmonic tuning capability of the one-port composite right-/left-handed transmission line (CRLH TL) [14], as illustrated in Fig. 1(b). We demonstrate that the newly designed PAs result in circuit sizes nearly one order of magnitude smaller than those of previous works, while still maintaining performance as continuously harmonic-tuned PA, as shown in Fig. 2. This paper extensively builds up on our previous work [15]. Firstly, we elaborate on a method of efficiently determining the design space parameters for continuous mode PAs, taking into account the FET parasitic network, a detail not described in [15]. Secondly, while [15] solely treated CCF PA, this study delves into the impact of PA operation modes, CCF or CCF⁻¹, on overall PA performance.

Load conditions setting

Ideal transistor

The theoretical load conditions for CCF and CCF⁻¹ PAs were derived by previous workers based on ideal transistors. For CCF PA, the load impedances for the fundamental frequency f_0 and the harmonic frequencies ($2f_0$ and $3f_0$) can be given as [9]

$$Z_{L1}(\gamma) = (2/\sqrt{3}) R_L^{opt} + jR_L^{opt} \gamma, \tag{1a}$$

$$Z_{L2}(\gamma) = -j(7\sqrt{3}\pi/24) R_L^{opt} \gamma, \tag{1b}$$

$$Z_{L3}(\gamma) = \infty, \tag{1c}$$

where γ is a dimensionless parameter ($-1 \leq \gamma \leq 1$) that determines the voltage waveform of the FET. The voltage waveform corresponds to that for a standard Class-F PA when $\gamma = 0$, but it becomes distorted as γ takes on non-zero values. However, this family of different voltage waveforms still offers the same power efficiency as the standard Class-F PA, thereby expanding the design space for Class-F PAs. R_L^{opt} is the optimum load impedance for ideal Class-B amplifier:

$$R_L^{opt} = \frac{V_D}{I_m/2}, \tag{2}$$

where V_D is the drain voltage and I_m is the maximum current of the FET.

As for the CCF⁻¹ PA, the theoretical load admittances for f_0 , $2f_0$, and $3f_0$ are [8]

$$Y_{L1}(\xi) = G_{opt} (\sqrt{2}i_1 - j\sqrt{2}i_{DC}\xi), \tag{3a}$$

$$Y_{L2}(\xi) = jG_{opt}2(i_1 + i_3)\xi, \tag{3b}$$

$$Y_{L3}(\xi) = \infty, \tag{3c}$$

where ξ ($-1 \leq \xi \leq 1$) is a parameter similar to γ in the CCF PA. However, unlike γ , ξ distorts the current waveform of the FET from that of a standard CCF⁻¹ PA when $\xi = 0$. Other parameters are given as follows: $G_{opt} = 1/R_L^{opt}$, $i_{DC} = 0.37$, $i_1 = 0.43$, $i_3 = 0.06$.

Figure 3 shows the typical theoretical load impedances (or load admittances) of (1) and (3) plotted on the Smith Chart. By relating

the values of γ or ξ to different frequency points within the desired frequency band, (1) and (3) now provide frequency-dependent load conditions to sustain the high efficiency of Class-F or Class-F⁻¹ amplifiers across the band. When considering real FETs with parasitic networks, however, the situation is not as straightforward, as discussed next.

Transistor with parasitic network

The discussion here pertains to a CCF amplifier unless otherwise specified, and similar discussion applies to a CCF⁻¹ amplifier. In the following, simulations were conducted using Keysight ADS, and the transistor model used was the nonlinear model provided by the manufacturer. As illustrated in Fig. 1, a real FET has parasitic network associated with both the device itself and its packaging. Basically, the load impedances at the intrinsic FET plane (Z_L^{int}) must satisfy the g -dependent theoretical load conditions (1a), (1b), and (1c). The load impedances at the extrinsic FET plane (Z_L^{ext}) are then determined as a function of frequency by projecting Z_L^{int} onto the extrinsic FET plane, utilizing the FET parasitic network model along with a given γ -frequency relationship (hereafter referred to simply as $\gamma(f)$). However, this approach to handling the impedances often results in Z_L^{ext} with a frequency response that cannot be realized using practical circuits. Therefore, we follow the subsequent design steps for determining Z_L^{ext} :

Step 1: Optimize $\gamma(f)$ so that the 2nd harmonic load $Z_L^{ext}(2f_0)$ rotates clockwise in the Smith Chart as the frequency increases.

Step 2: The function $\gamma(f)$ optimized in Step 1 causes the 3rd harmonic load $Z_L^{ext}(3f_0)$ to rotate counterclockwise as the frequency increases. Consequently, the values of $Z_L^{ext}(3f_0)$ are adjusted to ensure a clockwise frequency response.

Step 3: Perform a load-pull simulation to determine the fundamental load $Z_L^{ext}(f_0)$, based on $Z_L^{ext}(2f_0)$ and $Z_L^{ext}(3f_0)$ established in Step 1 and Step 2, respectively.

In Step 1, we focus on $Z_L^{ext}(2f_0)$ rather than $Z_L^{ext}(f_0)$ for the following reason: As shown in Fig. 3, the load impedances for the fundamental and 2nd harmonic frequencies tend to move in the opposite directions. This arises from the fact that, in (1a) and (1b), the terms associated with the parameter γ exhibit opposite signs. Consequently, when projecting the γ -dependent impedances to the frequency-dependent loads at the extrinsic plane, there is a possibility that either $Z_L^{ext}(f_0)$ or $Z_L^{ext}(2f_0)$ may rotate counterclockwise as the frequency increases. However, achieving a counterclockwise frequency response of impedance using practical circuits is challenging, especially when the impedance is on the edge of the Smith Chart, as in the case of $Z_L^{ext}(2f_0)$. Therefore, we determine the γ -frequency relationship, in such a way that $Z_L^{ext}(2f_0)$ rotates clockwise as the frequency increases. The method for handling $Z_L^{ext}(f_0)$ is discussed in Step 3.

In Fig. 4, two examples of $\gamma(f)$ function are illustrated, one being optimized and the other nonoptimized. The optimized $\gamma(f)$ led to a clockwise rotation of $Z_L^{ext}(2f_0)$, while the nonoptimized $\gamma(f)$ caused a counterclockwise rotation. It can be seen that even a minor difference in $\gamma(f)$ leads to significant variations in the frequency response of $Z_L^{ext}(2f_0)$. Therefore, instead of relying on a trial-and-error approach to find the optimal $\gamma(f)$ [3, 5], we used design charts, as shown in Fig. 5. Each chart consists of a series of curves representing the frequency response of $Z_L^{ext}(2f_0)$ for CCF PA and CCF⁻¹ PA. These curves are computed based on the detailed FET parasitic network model for the CGH40010F device

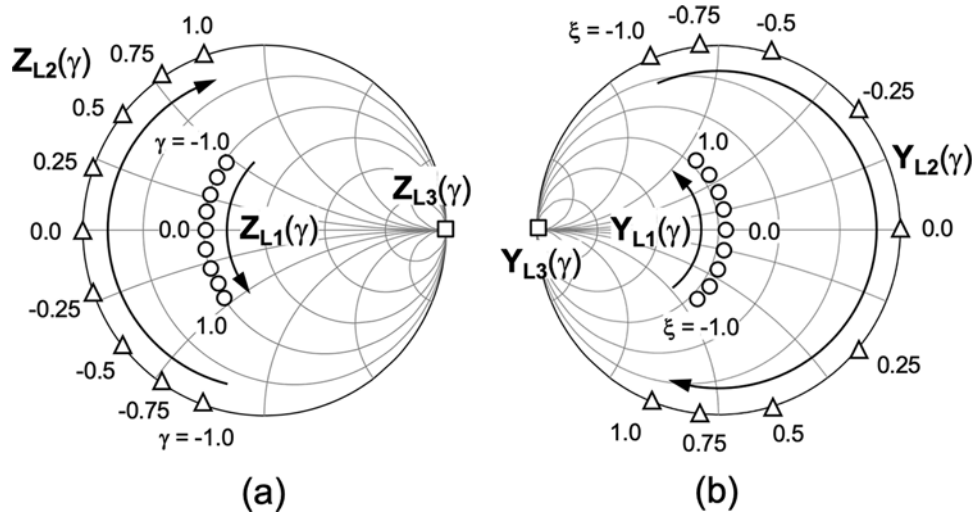


Figure 3. Fundamental and harmonic load conditions for (a) CCF and (b) CCF⁻¹ amplifiers using ideal FETs.

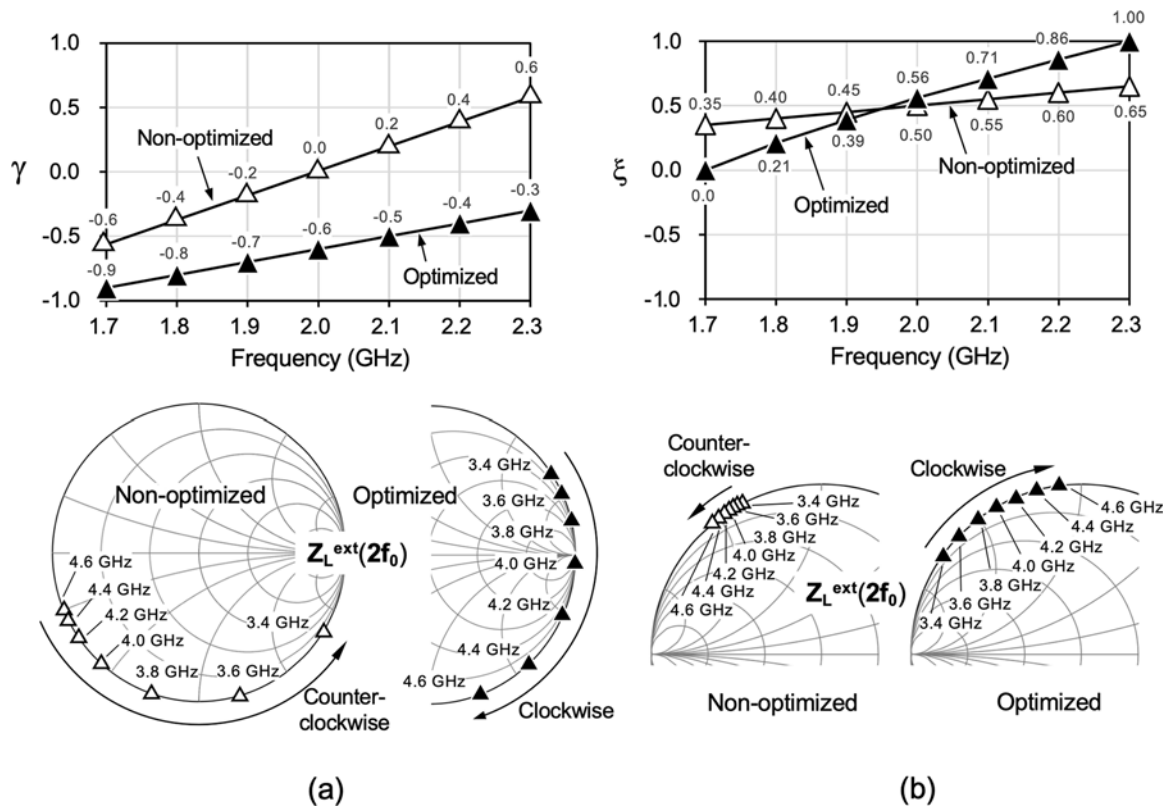


Figure 4. Design space parameters, γ and ξ , for (a) CCF and (b) CCF-1 amplifiers as a function of frequency. The bottom illustrates the effect of γ and ξ on the frequency variation of the external 2nd harmonic load impedance.

[2]. As can be seen from Fig. 5, each pair of curves for the same γ value exhibits divergent behavior at a certain frequency pole. To better understand the behavior of $Z_L^{ext}(2f_0)$, we derived an analytical expression for $Z_L^{ext}(2f_0)$:

$$Z_L^{ext}(2f_0) = j \cdot \left(\frac{R_L^{opt}}{\omega C_p R_L^{opt} - \frac{24}{7\sqrt{3}\gamma}} - \omega L_p \right), \quad (4)$$

which is based on a simplified FET parasitic network consisting of C_p and L_p (Fig. 1). From (4), it is evident that the parasitic elements

introduce a frequency pole in $Z_L^{ext}(2f_0)$. This frequency pole, which depends on γ , complicates the relationship between the load impedances at the intrinsic and the extrinsic planes. Consequently, it becomes challenging to predict the effect of the $\gamma(f)$ function on the frequency response of $Z_L^{ext}(2f_0)$ without referring to the design chart provided in Fig. 5.

In Step 2, we determine the third harmonic load, $Z_L^{ext}(3f_0)$. According to (1c), the ideal load conditions of Z_{L3} exhibit no frequency dependence. However, once projected on to the external FET plane through the parasitic network, it displays a frequency

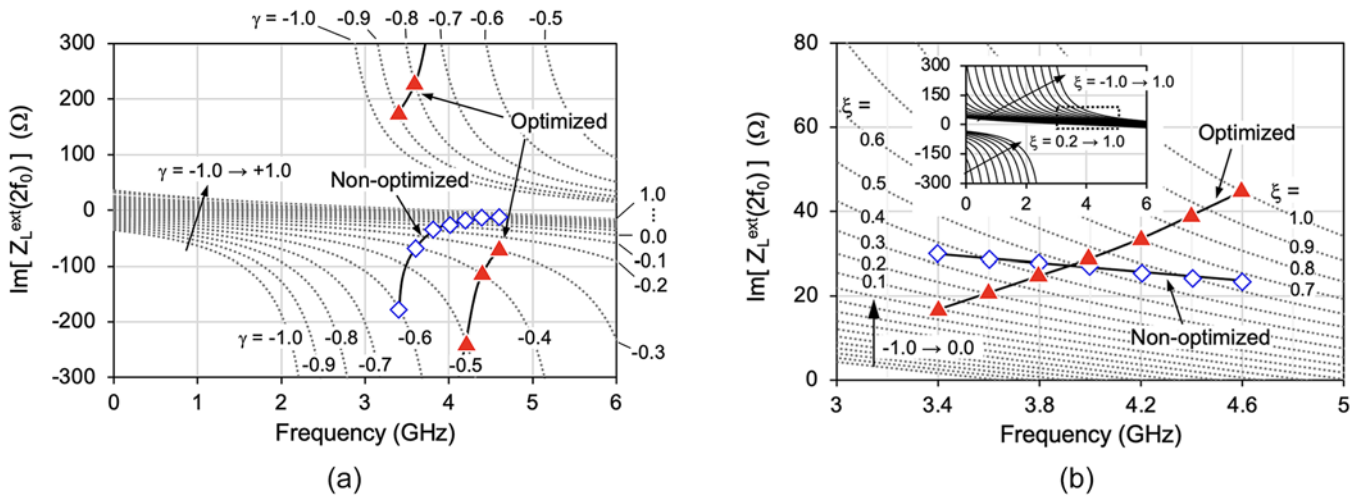


Figure 5. Design charts for determining (a) γ -frequency relation for CCF PA and (b) ξ -frequency relation for CCF⁻¹ PA.

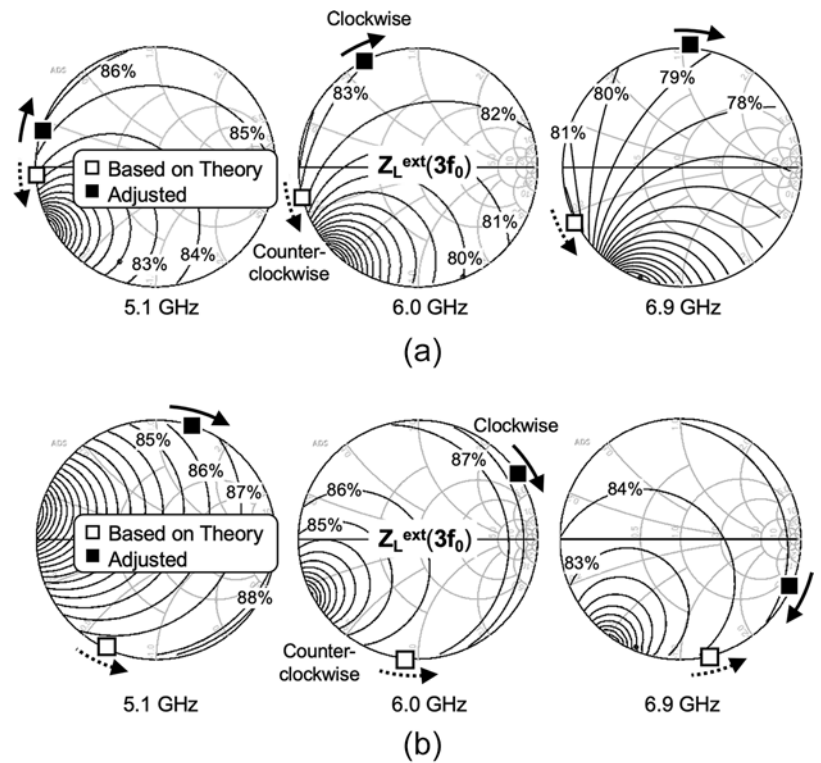


Figure 6. Method of determining the 3rd harmonic loads for (a) CCF PA and (b) CCF⁻¹ PA.

response of counterclockwise rotation, as indicated by the open rectangles in Fig. 6. Therefore, we adjusted the load impedances at each frequency points to ensure clockwise rotation of the impedance, as shown by the solid rectangles. Throughout this process, there is no need to compromise on achievable efficiency because the power-added efficiency (PAE) is relatively insensitive to the load near the maximum efficiency point, as evidenced by the PAE contours, also shown in Fig. 6.

In Step 3, we determine the remaining $Z_L^{ext}(f_0)$. In obtaining $Z_L^{ext}(f_0)$, we do not rely on the theory of (1), as we did in Step 1 to obtain $Z_L^{ext}(2f_0)$. This is because, even if we disregard the parasitic network of the transistor, the transistor still exhibits a knee voltage in its I-V characteristics, making it impossible to

determine $Z_L^{ext}(f_0)$ without accounting for this factor. Therefore, we obtain $Z_L^{ext}(f_0)$ using load-pull simulation while maintaining $Z_L^{ext}(2f_0)$ and $Z_L^{ext}(3f_0)$ at values determined in Step 1 and Step 2, respectively. Figure 7 shows the trajectory of $Z_L^{ext}(f_0)$ obtained by load-pull simulation as the frequency f_0 is swept from 1.7 GHz to 2.3 GHz (solid circles). For comparison, the impedances of $Z_L^{ext}(f_0)$ based on theory, i.e. using (1a) with the $\gamma(f)$ established in Step 1, are also shown (open circles). It can be seen that the load-pull simulation result demonstrates an impedance trajectory close to the theoretical prediction. The difference between the two trajectories is considered to reflect the effect of the knee voltage on the optimum load line. Although the desired load $Z_L^{ext}(f_0)$ rotates counterclockwise with increasing frequency, it is possible to approximate

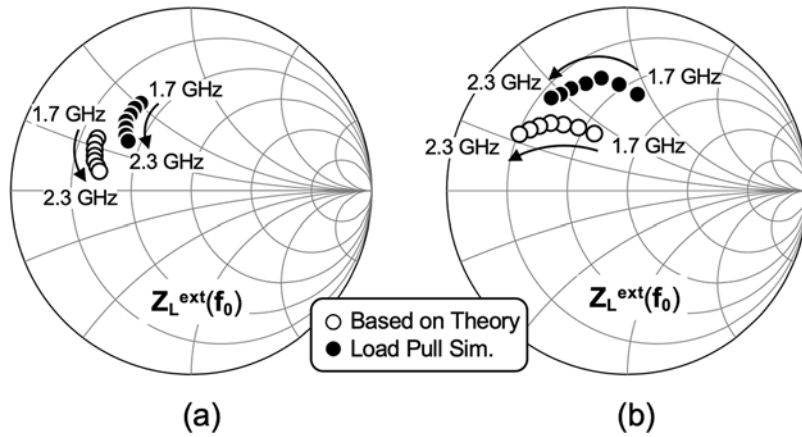


Figure 7. Frequency variation of optimum fundamental loads for (a) CCF PA and (b) CCF⁻¹ PA.

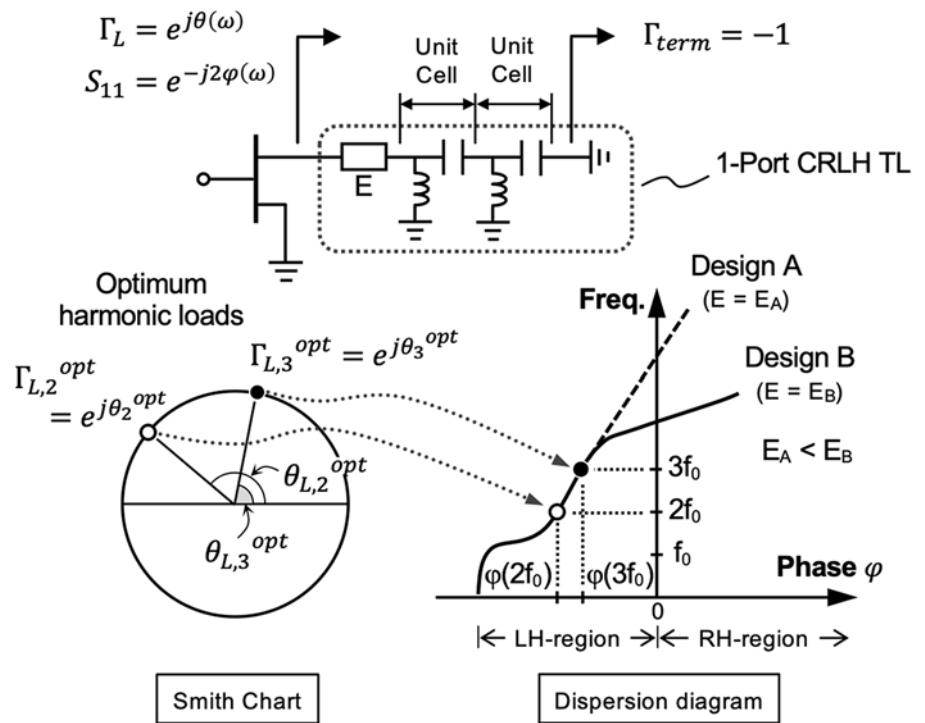


Figure 8. Conceptual illustration of an FET harmonically loaded with a one-port CRLH TL.

their trajectory using a clockwise impedance path achieved by a circuit with minimal mismatch, because the impedance varies within a relatively small area in the Smith Chart.

Principle of one-port CRLH transmission line

As illustrated in Fig. 1(b), at harmonic frequencies, the CRLH TL is isolated from the fundamental load, thus effectively functioning as a one-port network. Therefore, let us consider Fig. 8, a conceptual illustration of an FET harmonically loaded with a one-port CRLH TL, which is applicable only at harmonic frequencies. The property of CRLH TL can be characterized by their dispersion diagram (phase–frequency relationship). For two-port CRLH TLs, the dispersion characteristics can be obtained using the Bloch–Floquet’s theorem as:

$$\varphi(f) = \cos^{-1} \left(\frac{1 - S_{11}S_{22} + S_{12}S_{21}}{2S_{21}} \right), \tag{5}$$

This implies that a bandgap exists if the value within the bracket in the right-hand side exceeds unity over a specific frequency range. For a two-port CRLH TL that is lossless ($|S_{21}| = |S_{12}| = 1$), reciprocal ($S_{21} = S_{12}$), and matched to the port reference impedances ($S_{11} = S_{22} = 0$), (5) simplifies to

$$S_{21} = e^{-j\varphi(f)}, \tag{6}$$

which is practically used to obtain the dispersion characteristics, $\varphi(f)$ (p. 88 in [16]). Since (6) is a familiar equation in the classical transmission line theory, it is natural to define the dispersion characteristics for one-port CRLH TL as [14]:

$$S_{11} = e^{-j2\varphi(f)} \cdot \Gamma_{term}, \tag{7}$$

where Γ_{term} (reflection coefficient at the terminal point of the CRLH TL) is 1 or -1 for open-ended or short-ended TL, respectively. While (6) remains valid for a two-port CRLH TL under limited conditions, (7) consistently holds true for a one-port CRLH TL, as long as it is lossless.

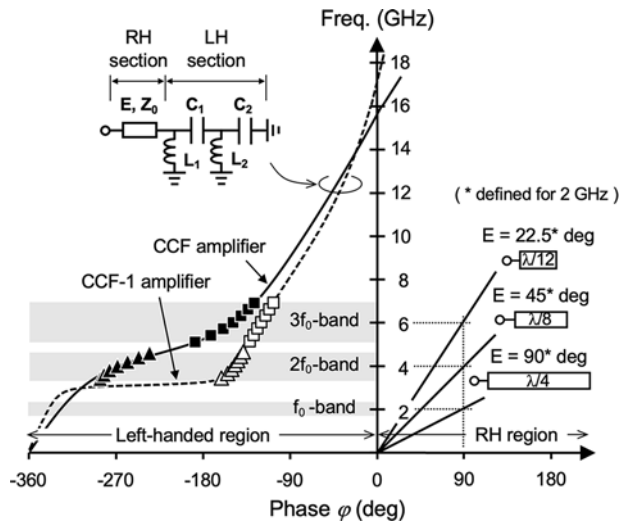


Figure 9. Dispersion characteristics of one-port CRLH Tls.

One of the most notable advantages of employing a one-port CRLH TL is the substantial increase in design flexibility compared to two-port CRLH TLs, which have significant design constraints. For instance, it is unnecessary to utilize repetitive identical unit cells as in the case of two-port CRLH TLs, where the transmission of signals between two ends must be ensured. Here, it is noted that periodicity is not a necessity for left-handed (LH) metamaterial theory [16]. Additionally, there is no need to address the bandgap issues when utilizing a one-port CRLH TL.

Now, as a nature of one-port network, the CRLH TL provides loads of pure reactance. Let us proceed to express the optimum harmonic loads for an FET with reflection coefficients:

$$\Gamma_{L,i}^{opt} = e^{j\theta_{L,i}^{opt}}, \tag{8}$$

where $i (= 2, 3)$ stands for the order of the harmonics. Meanwhile, the dispersion characteristics $\varphi(f)$ of one-port CRLH TL can be given as (7) with $\Gamma_{term} = -1$. To ensure that the CRLH TL satisfies the specified harmonic load conditions, (7) must match (8). Therefore, our objective is to optimize the dispersion profile $\Gamma(f)$ so that it intersects the target points at $2f_0$ and $3f_0$ as follows:

$$\varphi(2f_0) = -\frac{1}{2}\theta_{L,2}^{opt} - \left(n_2 - \frac{1}{2}\right)\pi, \tag{6a}$$

$$\varphi(3f_0) = -\frac{1}{2}\theta_{L,3}^{opt} - \left(n_3 - \frac{1}{2}\right)\pi, \tag{6b}$$

where n_2 and n_3 are arbitrary integers.

Circuit design method

Output harmonic tuning

To implement the CRLH TL in the PAs for operation in CCF and CCF⁻¹, the parameters of CRLH TL were optimized for each operating mode. Figure 9 illustrates the dispersion characteristics for these CRLH TLs. The triangle and rectangle plots correspondingly represent the optimum load impedances for the 2nd and 3rd harmonic frequencies, as depicted in Figs. 4 and 6. The parameter values for the CRLH TLs are listed in Table 1. It is observed that the dispersion curve for each operating mode satisfies the specified

Table 1. Parameters for CRLH transmission lines

PA mode	C ₁ (pF)	C ₂ (pF)	L ₁ (nH)	L ₂ (nH)	E ^a (deg)	Z ₀ (W)
CCF	0.6	0.2	1.3	0.8	12	50
CCF ⁻¹	0.6	0.6	1.0	2.0	5	50

^aElectrical length based on 2 GHz.

harmonic load conditions. In this manner, the dispersion curve can accommodate various kinds of frequency variations in the load impedances, showcasing the wide range of applicability of the one-port CRLH TL.

As another advantage of the one-port CRLH TL, its size can be nearly freely manipulated while simultaneously ensuring it meets the specified harmonic load conditions. This is explained as follows: The gradient of the dispersion for the conventional TL (with RH electromagnetic property) is inversely proportional to the length of the TL, as illustrated on the right-hand side of Fig. 8. Thus, considering that the property of CRLH TL in the RH region is predominantly determined by the RH section of the CRLH TL, the length of the RH section can be reduced by increasing the dispersion gradient of the CRLH TL in the RH region. On the other hand, the harmonic loads are determined by the dispersion curve in the LH region of the diagram. This implies that the function and the size of the CRLH TL can be optimized almost independently of each other. From Table 1, it is evident that the lengths of the RH section for the two CRLH TLs are minimized, significantly shorter than $\lambda/12$ (where λ is the wavelength for the fundamental frequency). This is a result of the design strategy aimed at enhancing the dispersion gradient as the dispersion curves extend into the RH region.

Harmonics trap filter

The harmonic trap filter (HTF) is an essential part of the proposed PAs harmonic tuning method. To preserve the merit of the miniature-sized one-port CRLH TL, minimizing the dimensions of the HTF is crucial. Figure 10 illustrates two different designs for the harmonic tuning networks utilized in CCF and CCF⁻¹ PAs. In both designs, two transmission zeros (TZs) at $2f_0$ and $3f_0$ are utilized to trap the harmonics. The stubs employed to generate the TZs are designed as compact as possible by loading capacitors at the end of the stubs [17]. For example, in CCF PA, the stub responsible for shorting at $2f_0$ comprises an 8.6-deg transmission line (TL1) and a 1.5-pF capacitor, resulting in a substantial size reduction compared to the 45-deg stub length required without the capacitor loading technique. The reason we employed double stubs for shorting the harmonics is to increase the bandwidth.

Apart from the shared features described above, different circuit topologies were employed for the HTFs in CCF and CCF⁻¹ PAs. In the case of CCF PA, a portion of the CRLH TL, specifically the branch line consisting of components C_1 , L_2 , and C_2 , is utilized for trapping $3f_0$, thus reducing the overall size of the harmonic tuning network. Here, the characteristics of the CRLH TL in the $3f_0$ band is determined by the RH section of the CRLH TL. Conversely, for CCF⁻¹ PA, the CRLH TL and the HTF are designed separately. Although the entire harmonic tuning network occupies slightly more circuit area compared to its counterpart in the CCF PA, this setup allows for individual optimization of both the CRLH

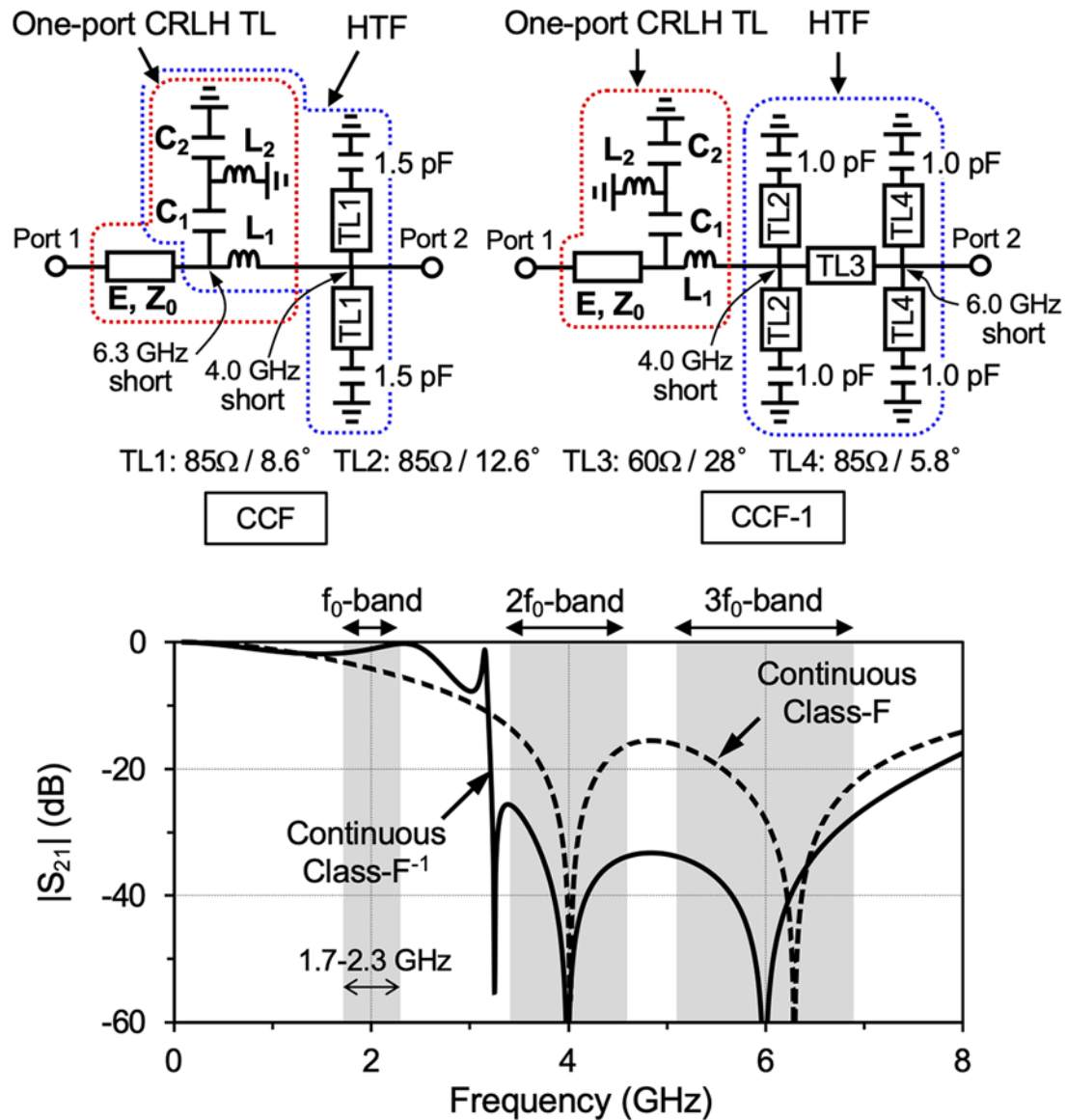


Figure 10. Configurations and frequency responses ($|S_{21}|$) of harmonic tuning networks for CCF and CCF^{-1} PAs.

TL and HTF. As a result, the harmonic tuning network for the CCF^{-1} PA shows more ideal LPF characteristics compared to that for the CCF PA, as depicted in Fig. 10. However, both harmonic tuning networks appear to function well when actually used in the PAs, as we will see in the next section.

Input harmonic tuning

While tuning the output harmonics is effective for enhancing the efficiency of PAs, certain operation classes of the PA also require additional harmonic tuning on the input side. In [13], it has been shown that its significance becomes apparent if the 2nd harmonic load impedance at the intrinsic FET plane ($Z_L^{int}(2f_0)$) approaches short. In such cases, the 2nd harmonic component of the drain current is boosted and fed back to the input through the gate-to-drain parasitic capacitance, necessitating compensation for the feedback effect on the input side.

Figures 11(a) and 11(b) show the simulated PAE with varying 2nd harmonic source impedance, $\text{Im}[Z_S(2f_0)]$, for CCF and CCF^{-1} PAs, respectively. The inset in each graph illustrates the 2nd harmonic load impedances at the intrinsic FET plane. Figure 11 illustrates that not only is the range of $\text{Im}[Z_S(2f_0)]$ for maximum PAE narrow but also even a slight deviation from the PAE local maxima point results in significant degradation of efficiency due to the presence of a PAE local minima point nearby. This effect is much more pronounced for CCF PA than for CCF^{-1} PA because $Z_L^{int}(2f_0)$ for the former is located closer to the short. This indicates that controlling $\text{Im}[Z_S(2f_0)]$ is highly critical in designing CCF PA. For instance, at 4.4 GHz, the achievable efficiency is low unless $\text{Im}[Z_S(2f_0)]$ is set in the vicinity of the local maxima point of the PAE. However, this also implies that a slight increase in the frequency will result in a collapse of efficiency. Taking all of this into consideration, the values for $\text{Im}[Z_S(2f_0)]$ for both CCF and CCF^{-1} PAs were set to the triangle points depicted in Fig. 11(a) and 11(b), respectively.

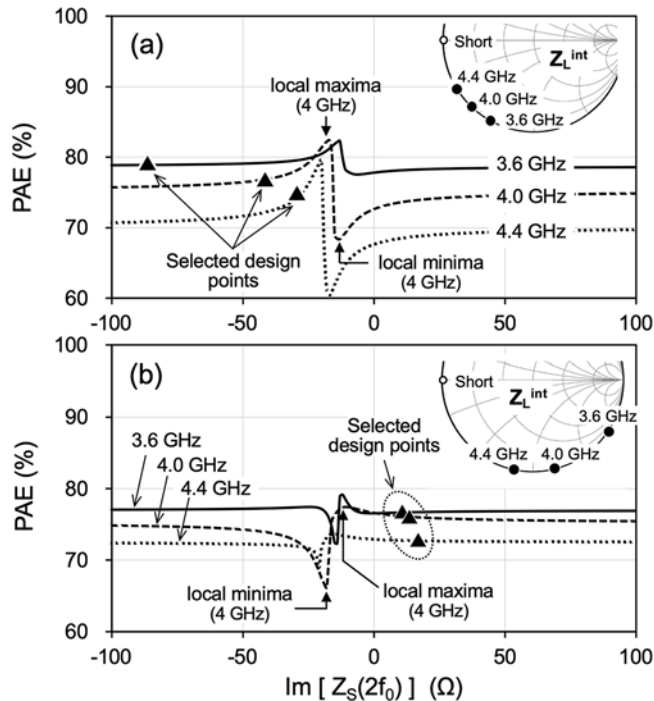


Figure 11. Simulated PAE with varying second harmonic source impedance for (a) CCF PA and (b) CCF⁻¹ PA.

Experimental results

PA fabrication

Figure 12 illustrates the configuration of the proposed PAs implemented in microstrip line (MSL) technology. The substrate utilized was Panasonic Megtron-6 R-5775 laminate ($\epsilon_r = 3.6$, $h = 0.63$ mm, $\tan\delta = 0.002$). For the CRLH TL, MSL inductors and 1005-size high-Q type chip capacitors (Murata, GJM series) were employed. The drain bias was provided via the inductor of the CRLH TL [12]. The LPF for the CCF PA was designed utilizing a stepped-impedance MSL. Since the LPF only needs to manage the fundamental frequency, a 2-stage filter design using TL sections with modestly low impedance ($Z_0 > 25 \Omega$) was deemed sufficient. In contrast, conventional continuous mode PAs typically utilized 3-stage filters using TL sections with very low impedance ($Z_0 < 10 \Omega$) [7, 9], as depicted by an image in Fig. 1(a). Regarding the CCF⁻¹ PA, an attempt was made to further reduce the total circuit size, by substituting lumped element capacitors of modest values (1.2 pF and 1.4 pF) for the low-impedance TL sections. Once again, this was made feasible due to the less stringent demand imposed on the LPF design compared to conventional continuous mode PAs.

Figure 13 shows the pictures of the fabricated PAs. The circuit layout was optimized using EM simulation. As can be seen from the picture, the footprints of the one-port CRLH TLs are remarkably small, comparable to that of the ceramic hermetic package of the FET. In this study, we define the effective circuit area of the PA as determined by the rectangles on both the input and output sides, encompassing only the essential part of the circuit (excluding components such as biasing circuits and DC-cut capacitors). As can be seen from Fig. 2, the effective circuit areas for the PAs of this work are significantly reduced compared to the conventional CCF and CCF⁻¹ PAs.

S-parameter measurement

Prior to assembling the PAs, the circuit boards on the input and output side were measured for S-parameters to verify if they meet the desired source/load conditions. Figure 14 compares the measured and simulated impedances for CCF and CCF⁻¹ PAs. The measurements reasonably align with the simulations. The fact that the measured load impedances in the $2f_0$ band (3.4–4.6 GHz) and those in the $3f_0$ band (5.1–6.9 GHz) precisely fall on the outer edge of the Smith Chart indicates that the harmonic trap filters for both CCF and CCF⁻¹ PAs are effectively functioning. As the frequency transitions from the high end of the f_0 band (2.3 GHz) to the low end of the $2f_0$ band (3.4 GHz), the desired load impedance shifts from the inner region to the outer edge of the Smith Chart. Since the load impedances at 2.3 GHz and 3.4 GHz for CCF⁻¹ PA are closely situated, designing the OMN for the CCF⁻¹ PA appears to be more challenging compared to the case of the CCF PA. However, despite the demanding conditions for CCF⁻¹ PA, the load impedance trajectory realized by the proposed circuit precisely adhered to the intended path from 2.3 GHz to 3.4 GHz. The rapid transition of the impedance from the inner region to the outer edge of the Smith Chart is realized if the harmonic trap filter is adequately designed.

Let us now shift our focus in Fig. 14 to the source impedances. In the Smith Chart, the PAE contours of the 2nd harmonic frequency of 4.0 GHz are shown as a reference. The local minima and maxima points exhibit minimal change with frequency variation, as depicted in Fig. 11. It can be observed that, for the CCF PA, the 2nd harmonic source impedance, $Z_S(2f_0)$, is controlled to avoid crossing the local minima at the high end of the targeted frequency band ($2f_0 = 4.6$ GHz). In other words, the bandwidth of the CCF PA is restricted by the design of the input matching network (IMN) considering the 2nd harmonic source impedance. In contrast, it is relatively straightforward to design the IMN for the CCF⁻¹ PA, because the efficiency decreases only minimally even if the impedance is apart from the local maxima, as demonstrated in Fig. 11(b).

Figure 15 shows the typical frequency responses of $|S_{21}|$ and $|S_{11}|$ measured for the CCF PA. While $|S_{21}|$ exceeds -20 dB at certain points within the frequency ranges corresponding to the 2nd and 3rd harmonic bands, specifically 3.4–4.6 GHz and 5.1–6.9 GHz, it remains predominantly below -20 dB. This result indicates that the HTFs are functioning as intended and confirms that the CRLH TLs effectively operate as one-port TLs, as anticipated.

Power measurement

Figure 16 shows the measured CW power performance for the fabricated CCF PA and CCF⁻¹ PA. For the CCF PA, at 1.8 GHz, the output power, drain efficiency (DE) and PAE reached 40.1 dBm, 79.5% and 75.6%, respectively. Meanwhile, the CCF⁻¹ PA achieved 41.2 dBm output power, 79.6% DE, and 74.0% PAE at 1.9 GHz. Figure 17 plots the maximum DE and PAE for the two types of PAs as a function of the frequency. Both types of the PAs exhibited a similar high-efficiency operational bandwidth. The bandwidth within which the PA operates with DE $> 70\%$ were 630 MHz and 620 MHz for CCF and CCF⁻¹ PA, respectively. Table 2 and Fig. 2 demonstrate that the bandwidths achieved by the proposed CCF and CCF⁻¹ PAs are comparable to those of the state-of-the-art PAs, despite the remarkable reduction in circuit size.

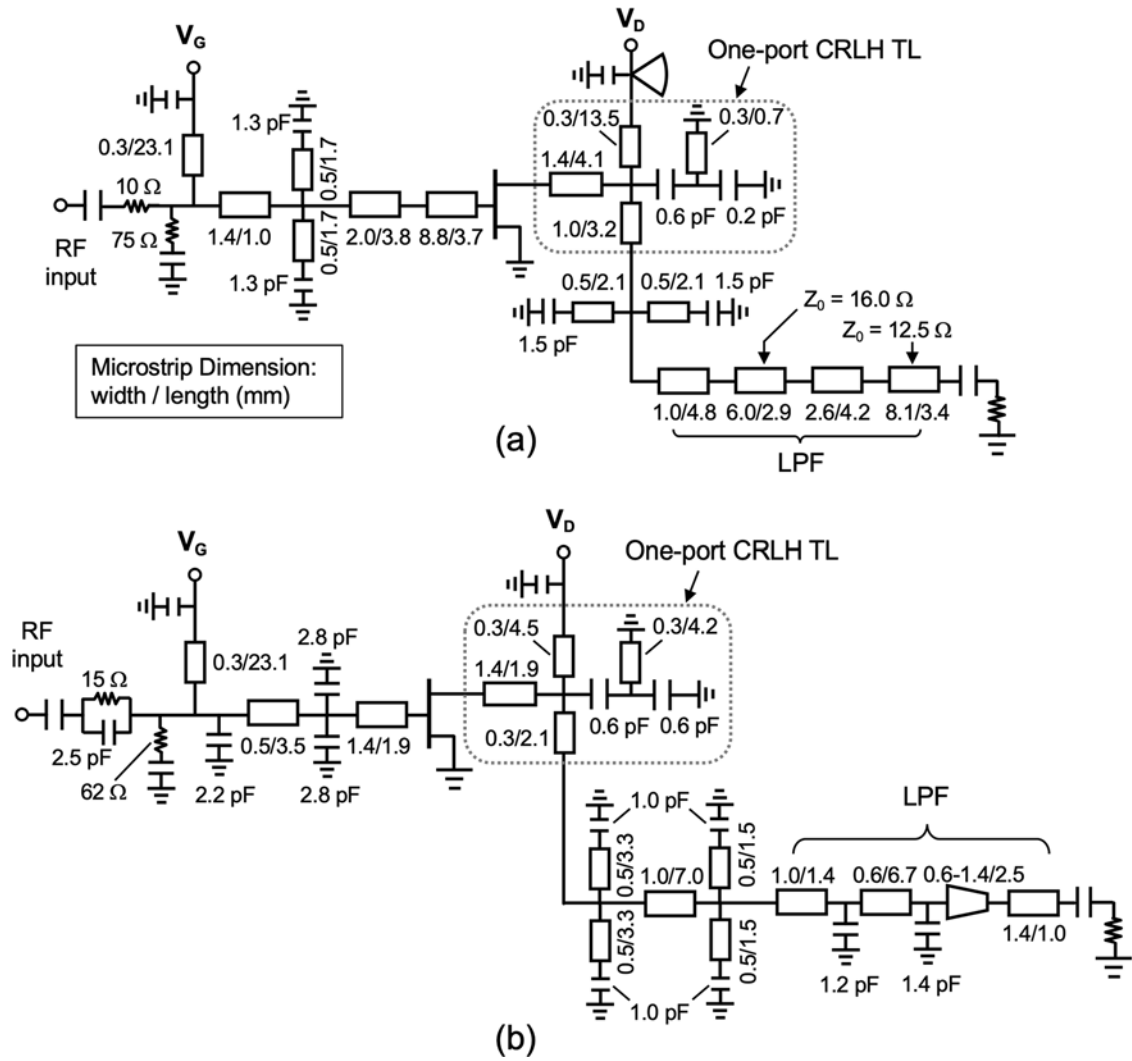


Figure 12. Configurations of the fabricated (a) CCF PA and (b) CCF⁻¹ PA.

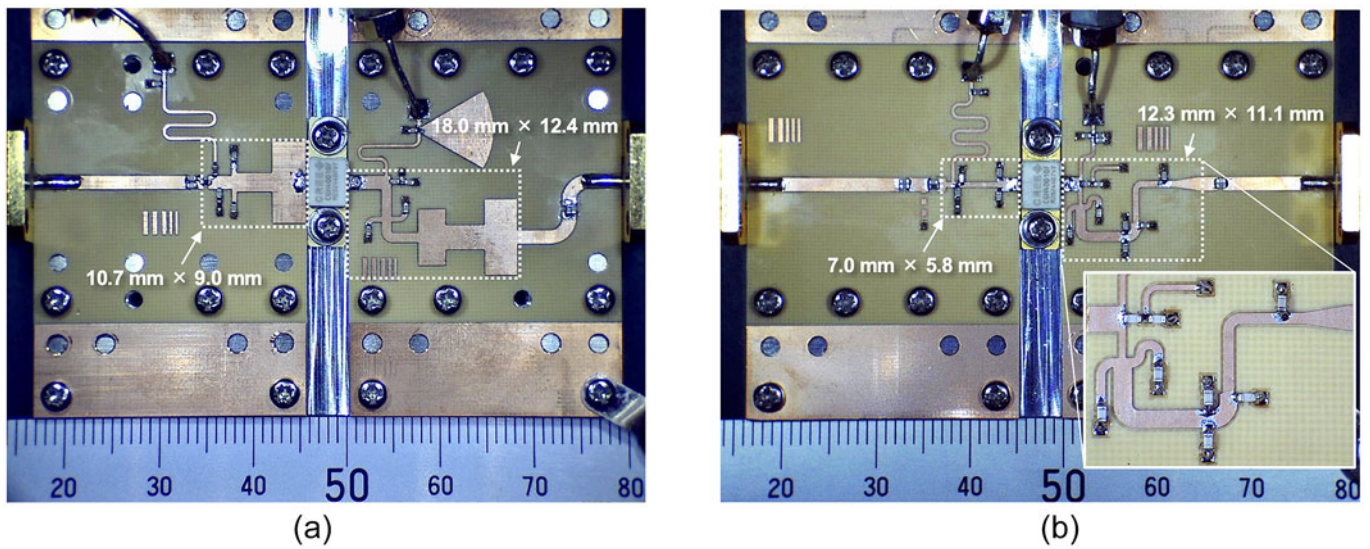


Figure 13. Photographs of the fabricated (a) CCF PA and (b) CCF⁻¹ PA.

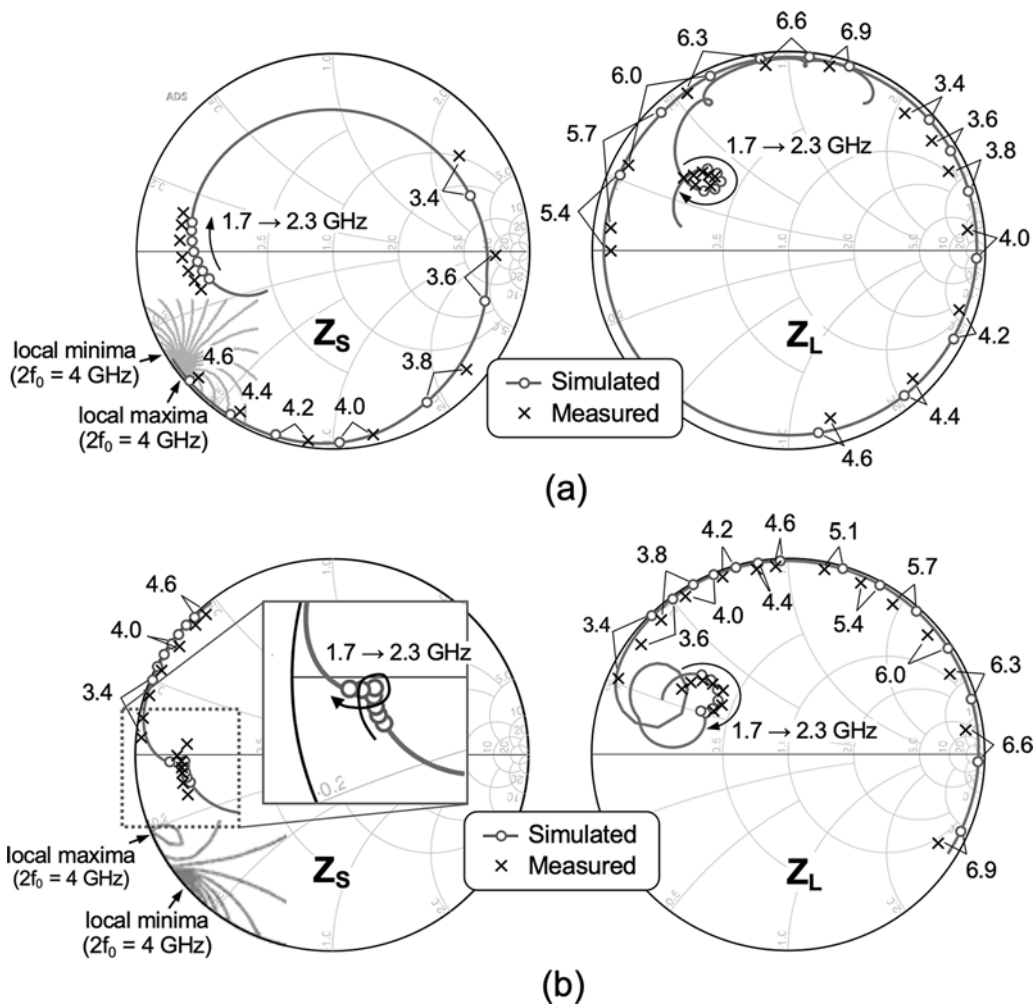


Figure 14. Measured and simulated impedances for IMNs and OMNs of the proposed (a) CCF PA and (b) CCF⁻¹ PA.

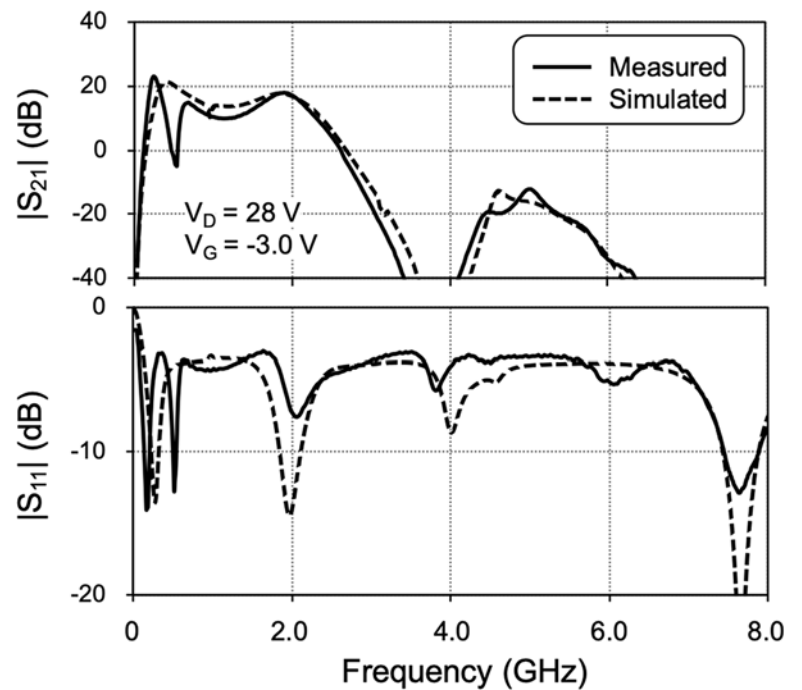


Figure 15. Measured S-parameters for CCF PA.

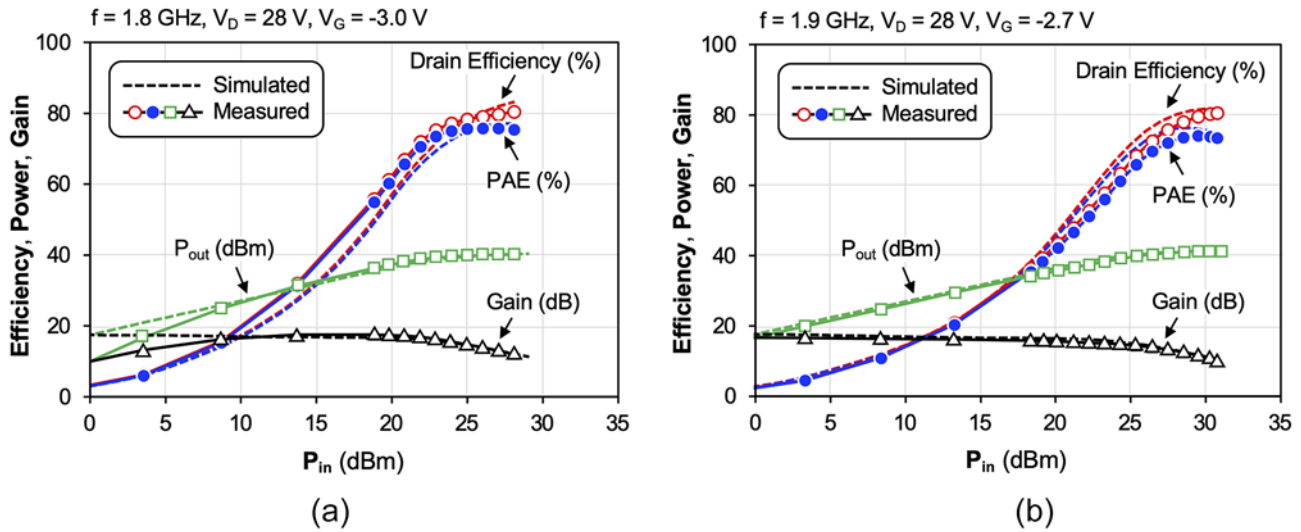


Figure 16. Measured power performance for proposed (a) CCF PA and (b) CCF⁻¹ PA.

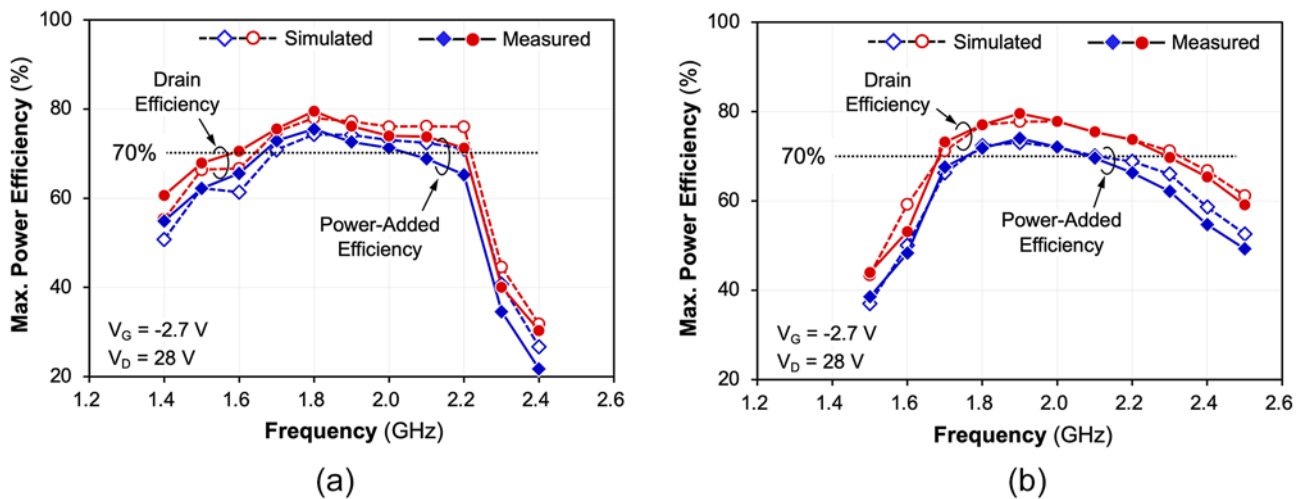


Figure 17. Frequency variation of efficiency for (a) CCF PA and (b) CCF⁻¹ PA.

Table 2. Comparison of state-of-the-art broadband high-efficiency PAs

Ref.	Operating Class	>70% Efficiency Operational Frequency Band (GHz)		Peak Value		Output MatchingNetwork	
		(DE)	(PAE)	(PAE)	(P _{out})	(e _r)	(Circuit Topology)
[9]	CCF/CCF ⁻¹	1.48 – 2.203.04 – 2.51	1.72 – 2.102.96 – 2.59	77%*	11 W	2.2	3-stage LPF
[7]	CCF ⁻¹	1.83 – 2.49	NA	80%	19.5 W	3.5	3-stage LPF
[8]	CCF ⁻¹	1.35 – 1.98	NA	NA	18 W	3.5	3-stage LPF
[2]	CCF	1.45 – 2.45	1.49 – 1.631.77 – 2.07	74%*	16.8 W	3.5	3-stage LPF
[4]	CCF	0.51 – 1.06	0.54 – 1.01	81%	13.2 W	3.4	3-stage LPF
This Work	CCF	1.64 – 2.21	1.67 – 2.02	76%	10.2 W	3.6	CRLH TL& 2-stage LPF
This Work	CCF ⁻¹	1.68 – 2.30	1.76 – 2.10	74%	13.2 W	3.6	CRLH TL& 2-stage LPF

*Estimated from graph.

However, notwithstanding the similarity regarding the bandwidth between the two PAs, there is a distinct difference in the efficiency behavior. While the efficiency of the CCF⁻¹ PA gradually decreased with frequency above 2.2 GHz, the efficiency of the

CCF PA collapsed at a frequency of around 2.2 GHz. The behavior of the CCF PA was expected because it was anticipated that the 2nd harmonic source impedance would intersect the point of local efficiency minima as the frequency is increased, as depicted

in Fig. 11(a). Thus, this is the main reason why we targeted a high-efficiency operational bandwidth of 1.7–2.3 GHz—it was challenging to ensure that $\text{Im}(Z_S(2f_0))$ did not intersect with the local efficiency minima before reaching a frequency of 2.4 GHz. In this regard, the CCF^{-1} PA had the potential to achieve a wider bandwidth, as the management of $\text{Im}(Z_S(2f_0))$ was less stringent. However, for the CCF^{-1} PA investigated in this study, the fundamental load at 2.3 GHz (the high end of the f_0 band) was very close to the 2nd harmonic load at 3.4 GHz (the low end of the $2f_0$ band). Consequently, this led to constraints for designing the LPF for fundamental frequency matching, resulting in decreased efficiency for frequencies less than 1.7 GHz (Fig. 17(b)). The issue may be alleviated by adjusting the $\xi(f)$ function so that the 2nd harmonic loads are placed similarly to the case of CCF PA (see Fig. 15), but addressing this issue remains a subject of our future work. Overall, while both the CCF PA and CCF^{-1} PA ultimately exhibited nearly the same high-efficiency operational bandwidths, it was found that the factors fundamentally limiting the bandwidth are different.

Conclusion

High-efficiency PAs with broadband characteristics are highly sought after for next-generation wireless systems. While the concept of continuous harmonic tuning presents a promising approach to achieving such PAs, the significant circuit size overhead of conventional designs has presented challenges for their practical application. Based on the demonstrated physical dimensions and the performance of the fabricated CCF and CCF^{-1} PAs, the proposed technique is expected to facilitate the adoption of continuous mode PAs for a variety of applications.

Acknowledgement. The authors would like to thank Prof. Emeritus K. Honjo of The University of Electro-Communications for helpful comments and discussions. This work was supported by JSPS KAKENHI (Grant Number 21K04181).

Conflict of Interest. None declared.

References

- Cripps SC, Tasker PJ, Clarke AL, Lees J and Benedikt J (2009) On the continuity of high efficiency modes in linear RF power amplifiers. *IEEE Microwave and Wireless Components Letters* **19**(10), 665–667. 10.1109/LMWC.2009.2029754
- Tuffy N, Guan L, Zhu A and Brazil TJ (2012) A simplified broadband design methodology for linearized high-efficiency continuous Class-F power amplifiers. *IEEE Transactions on Microwave Theory & Techniques* **60**(6), 1952–1963. 10.1109/TMTT.2012.2187534
- Aggrawal E, Rawat K and Roblin P (2017) Investigating continuous class-F power amplifier using nonlinear embedding model. *IEEE Microwave and Wireless Components Letters* **27**(6), 593–595. 10.1109/LMWC.2017.2701316
- Zheng SY, Liu ZW, Zhang XY, Zhou XY and Chan WS (2018) Design of ultrawideband high-efficiency extended continuous class-F power amplifier. *IEEE Transactions of Industrial Electronics* **65**(6), 4661–4669. 10.1109/TIE.2017.2772163
- Liu G, Mu G, Qiu X, Leng Y and Peng X (2019) Design of broadband power amplifier based on continuous class-F mode with frequency parameterization. *IEICE Electronics Express* **16**(6), 1–4.
- Carrubba V, Akmal M, Quay R, Lees J, Benedikt J, Cripps SC and Tasker PJ (2012) The continuous inverse Class-F mode with resistive second-harmonic impedance. *IEEE Transactions on Microwave Theory & Techniques* **60**(6), 1928–1936. 10.1109/TMTT.2012.2189228
- Sun Y and Zhu X (2015) Broadband continuous class-F⁻¹ amplifier with modified harmonic-controlled network for advanced long term evolution application. *IEEE Microwave and Wireless Components Letters* **25**(4), 250–252. 10.1109/LMWC.2015.2400941
- Yang M, Xia J, Guo Y and Zhu A (2016) Highly efficient broadband continuous inverse class-F power amplifier design using modified elliptic low-pass filtering matching network. *IEEE Transactions on Microwave Theory & Techniques* **64**(5), 1515–1525. 10.1109/TMTT.2016.2544318
- Chen K and Peroulis D (2012) Design of broadband highly efficient harmonic-tuned power amplifier using in-band continuous Class-F⁻¹/F mode transferring. *IEEE Transactions on Microwave Theory & Techniques* **60**(12), 4107–4116. 10.1109/TMTT.2012.2221142
- Chen H, Xu J-X, Kong Z-H, Chen W-H and Zhang XY (2020) Broadband high-efficiency power amplifier with quasi-elliptic low-pass response. *IEEE Access* **8**, 52566–52574. 10.1109/ACCESS.2020.2980688
- Chen K and Peroulis D (2013) A 3.1-GHz class-F power amplifier with 82% power-added-efficiency. *IEEE Microwave and Wireless Components Letters* **23**(8), 436–438. 10.1109/LMWC.2013.2271295
- Tanaka S, Oda T and Saiki K (2019) Novel DC-biasing circuits with arbitrary harmonics-control capability for compact high-efficiency power amplifiers. *International Journal of Microwave and Wireless Technologies* **11**(7), 618–624. 10.1017/S1759078719000473
- Tanaka S, Asami H and Suzuki T (2022) Class-E power amplifier with improved PAE bandwidth using double CRLH TL stub for harmonic tuning. *IEICE Transactions on Electronics* **E105-C**, 441–448. 10.1587/transele.2022MMI0002
- Tanaka S, Mogami R, Iisaka N, Honjo K and Ishikawa R (2024) A 2-GHz GaN HEMT power amplifier harmonically tuned using a compact one-port CRLH transmission line. *IET Circuits, Devices and Systems* **2024**, Article ID 2690713. 10.1049/2024/2690713
- Tanaka S and Tsuji E: A 1.6-2.2 GHz Continuous Class-F Power Amplifier with Compact Harmonically Controlled Networks, *European Microwave Conference*, 504–507, Milan, 2022. 10.23919/EuMC54642.2022.9924488
- Caloz C and Itoh T (2005) *Electromagnetic Metamaterials: Transmission Line Theory and Microwave Applications*. New York: Wiley.
- Tanaka S, Katayose T, Nishizawa H, Hosoya K, Ishikawa R and Honjo K (2016) Miniaturization of double stub resonators using lumped-element capacitors for MMIC applications. *IEICE Transactions on Electronics* **E99-C**(7), 830–836. 10.1587/transele.E99.C.830



Eri Tsuji received the B.E. degree in Communications Engineering and the M.E. degree in Electrical Engineering and Computer Science from Shibaura Institute of Technology in 2021 and 2023, respectively. In 2023, she joined Kyocera Corporation, Yokohama, Japan. Ms. Tsuji is a member of the Institute of Electrical, Information and Communication Engineers (IEICE), Japan.



Soshi Aonuma received the B.E. degree in Information and Communications Engineering and the M.E. degree in Electrical Engineering and Computer Science from Shibaura Institute of Technology in 2022 and 2024, respectively. In 2024, he joined Sumitomo Electric Industries, Ltd., Yamanashi, Japan. Mr. Aonuma is a member of the Institute of Electrical, Information and Communication Engineers (IEICE), Japan.



Shinichi Tanaka received the B.E. and M.E. degrees in Applied Physics from the University of Tokyo and the D.E degree in Electrical Engineering from Tohoku University, Sendai, in 1984, 1986 and 1997, respectively. In 1986, he joined the Central Research Laboratories, NEC Corporation, Kawasaki, Japan, where he was involved in the development of GaAs and InP HBTs and their applications to microwave and millimeter-wave ICs. From 1992 to 1993, he worked on modeling

and simulation of hetero-structure devices at Purdue University, West Lafayette, IN, as a Visiting Scholar. From 2005 to 2009, he was a Visiting Professor at the University of Electro-Communications, Tokyo. Since 2009, he has been a Professor at Shibaura Institute of Technology, Tokyo. He was a co-recipient of the APMC'99 Microwave Prize. Dr. Tanaka holds senior memberships in the IEEE, the Institute of Electrical, Information and Communication Engineers (IEICE), and the Institute of Electrical Engineers of Japan (IEEJ).